PANORAMIC IMAGING MONOCHROMATIC CAMERAS FOR REMOTE DIAGNOSTICS OF IONOSPHERE AND UPPER ATMOSPHERE FROM SATELLITES

A.K. Kuz'min and K.N. Chikov

Institute for Space Research, Russian Academy of Sciences, Moscow
Received May 4, 1994

Possibilities of methods for measurement of auroral characteristics and electrodynamical parameters of the polar ionosphere from satellites by means of the system of wide–angle imaging cameras using new modifications of the "monochromatic eye" objective are considered. Aberrational and spectral characteristics of the objectives and their relative advantages and shortcomings are analyzed. Conception of the system construction and of a choice of the upper atmospheric emission wavelength for simultaneous spectrophotometric measurements of the aurora intensity distributions over a wide spatial band from low–apogee satellites are presented. The advantages that the imaging cameras provide for remote diagnostics of the instantaneous states and for the study of the processes in polar ionosphere are discussed.

1. METHODOLOGICAL ASPECTS OF REMOTE DIAGNOSTICS OF THE IONOSPHERE USING MONOCHROMATIC IMAGES OF THE UPPER ATMOSPHERIC LIGHT EMITTING LAYERS

Mapping of the intensity distribution of the emission from upper atmospheric layers by means of both ground based photometric devices and spaceborn ones is considered to be a promising tool that could provide information about the basic parameters of polar ionosphere and enable remote diagnostics of its instantaneous state. Indeed, by analyzing intensity distribution of the upper atmospheric emissions in the image of the whole auroral oval and in its separate parts obtained in narrow spectral regions it is possible to identify regions where the intense ionospheric ionization and recombination processes occur. Those processes are related to injection of high–energy electrons and ions from magnetosphere as well as to longitudinal currents directed upward. Moreover, such a distribution enables one to calculate characteristic and average energy of the charged particles, energy flux related to their motion, ionospheric conductivity integrated over the altitude, etc., since emission intensity is known to be a measure of the relative amount of energy of the particles that reach certain altitudes in the atmosphere.[1–3]

The matter is that high–energy electrons and ions as well as secondary electrons excite atoms and molecules at a certain altitude in the upper atmosphere in a proportion to their relative amount at this altitude.

In Ref. 4 based on the data obtained from satellite DE–1 factors determining the relationship between the intensity distribution in a monochromatic image and the rate of the energy losses of auroral particles, their characteristic energy and the energy flux related to the injection of electrons, and ionospheric conductivities are discussed. Hall and Pedersen conductivity (Σ_h and Σ_p, respectively) integrated over the altitude are derived from a general solution of the energy equation and continuity equation with the aid of time–dependent models of the ionosphere and thermosphere. In these calculations, conductivity is obtained as a function of energy flux F_e and characteristic energy E_0 of the electrons injected.

This procedure has been being developed since seventieths. In Russia use of this technique started after successful spectrophotometric experiments on measurements of the aurora parameters from satellites Oreol–3 and IK–Bolgariya–1300[5,6] which were equipped with multichannel scanning photometers of second generation whose field–of–view angle is about several degrees. The next generation of aurora photometers uses coordinate–sensitive CCD matrices resulting in appreciably wider field–of–view angle of an instantaneous observation.

In wide–angle monochromatic imaging devices that are installed on foreign satellites during the last decade[7–13] and in the known new projects[14,15] flat interference filters with the transmission bandwidth ranging from several nanometers to several tens of nanometers are used for separation of specific atmospheric emissions. Location of the transmission band maximum for a flat filter is known to be dependent on the angle of incidence. Oblique incidence of light leads to a blue shift of the band maximum. Absolute value of the shift is proportional to the square of the incidence angle. Moreover, broadening of the band along with a reduction of the peak transmission occurs in this case.

Hence, absolute sensitivity of a wide–angle imaging photometer for any specific emission depends on the direction of observations. The fact that location of a transmission band maximum depends on temperature (≈□0.01–0.03 nm/°C) causes additional errors in relative intensities measured in different directions and results in determination of distribution of a number of electrodynamic parameters in the ionosphere to a rather low precision. This problem is especially severe for narrow–band visible imaging cameras limiting field–of–view angle and preventing from the employment of interference filters with the bandwidth of several fractions of nanometer even under conditions of good thermostabilization.

In an optical system with a wide–angle quasimonochromatic camera including "monochromatic eye" (ME) objective this problem is completely solved and new

0235-6880/95/6 466-06 $02.00

prospects for measurements of the auroral and ionospheric characteristics are evident (see below).

2. ADVANTAGES OF "MONOCHROMATIC EYE" OBJECTIVE USED IN A WIDE–ANGLE CAMERA

New versions of objective systems have been developed for the imaging cameras. They exhibit their own merits and shortcomings described below. Characteristics of first versions (ME–SV1 for the visible and ME–SU1 for the VUV) developed on the base of concentric optical systems[16] are the basic ones for a ME objective and have been considered and analyzed in details in Ref. 17. In this paper, two recent modifications of the ME objective, ME–SV2 and ME–SU2, are presented and characteristics of ME–PV objective for the visible are considered.

ME–SV2 objective is a four–component mirror and lens optical system whereas ME–SU2 is a five–component system. Both systems have a ring–shaped input aperture. A dualreflector––caridioidcondensor is the basic element in the first system whereas a triplereflector is the basic element in the second one. Both systems include meniscus compensator consisting of two meniscus *1* and *3* (see Figs. 1 and 2). Third component in ME–SU2 (spherical mirror *7* in Fig. 2) together with a flat mirror *8* is used for suppression of scattered solar light[18,19] when measurements are carried out in the illuminated part of the auroral oval. This mirror serves as an additional objective that projects focal surface of the main objective (dualreflector–caridioidcondensor *4* and *5*) onto the sensitive area of a radiation detector *9*. It should be stressed here that higher suppression of scattered light is achieved by the use of additional flat mirror *8* (see Fig. 2) that divides working volume of the objective into two optical cameras. It should be noted that only light passed through the hole in the flat mirror, or, in other words, through an intermediate field aperture, reaches the output camera and the radiation detector.

A ring–shaped input aperture of the objectives is caused by screening of their central parts by the convex mirror *4* depicted in Figs. 1 and 2. To minimize the screening the input aperture, in ME–SV2 and ME–SU2 in contrast to that of ME–SV1 and ME–SU1 it is combined with the above mentioned convex mirror *4*. The front meniscus doublet is concentric relative to the common curvature center located on the vertex of the convex mirror. Such a location of meniscus doublet provides for one and the same ray path through other optical elements of the objectives and allows one to keep the initial aberration level (see Ref. 17).

An important specific feature of ME–SV2 and ME–SU2 objectives is that the spherical interference filter *2* used for separation of emissions plays the role of the internal concave surface of the input concentric correcting meniscus *1* or with inner convex surface of the concentric correcting meniscus *2* which are used to correct for spherical aberrations. Common curvature center *C* of the interference layers and of both concentric surfaces of radii r_2 and r_3 coincides with the center of input aperture and, hence, the characteristics of the interference filter (transmission bandwidth, location of the band maximum) are independent of direction of the beam within the field of view. Concentric meniscus *1* serves also as an input window of the objective thus protecting interference filter against dangerous atmospheric and mechanical influence when being tested on the Earth and against direct radiation in space.

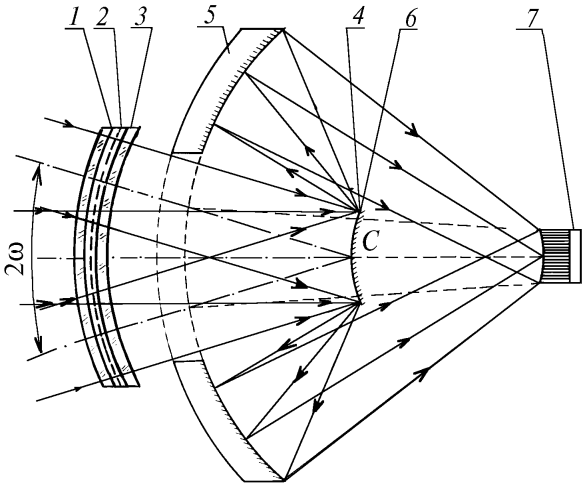

FIG. 1. Optical arrangement of an ME–SV2 objective for the visible region: input concentric correcting meniscus (meniscus compensator) (1), spherical interference filter (2), output concentric correcting meniscus (meniscus compensator) (3), convex mirror (4), main concave mirror (5), input pupil placed at the common curvature center of all optical surfaces C (6), fiber–washer or microchannel plate with a spherical input surface of radius $R = f'_\Sigma$ located infront of a radiation detector (CCD matrix) (7).

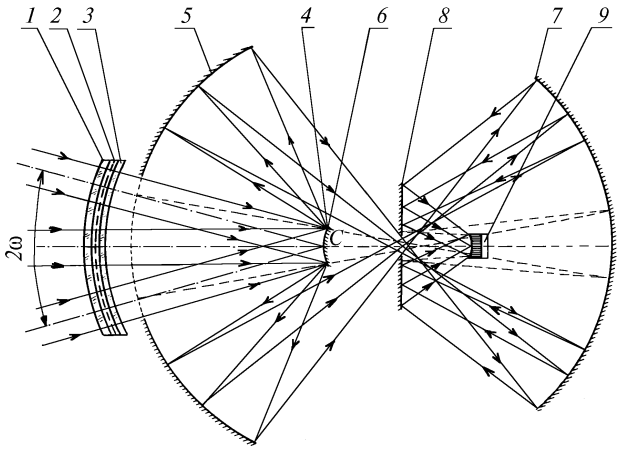

FIG. 2. Optical arrangement of an ME–SU2 objective for the VUV: 1–6 corresponds to the elements in Fig. 1, an additional concave mirror (7), a flat mirror (8), fiber–washer or microchannel plate with a spherical input surface of radius $R = f'_\Sigma$ located infront of a radiation detector (CCD matrix) (9).

This construction of optical system provides for a stable location of the transmission band maximum of the filter both at the center and in the periphery of the field of view. In our specific case, the field–of–view angle is $2\omega \approx 33°24'$ both for the visible and UV spectral regions (see Figs. 1 and 2). Preliminary calculations show that the transmission bandwidth at half maximum increases by 0.1–0.2 nm for the field–of–view periphery from its initial value of 1.5 nm on the axis. This deviation can be reduced by optimizing the number of interference layers and their characteristics. It is worth mentioning here that it is technically possible to obtain rather narrow band ($\delta\lambda \approx 5$–7 nm) of a flat filter in the VUV produced using a combination of several reflecting and transmitting multilayer packages.[20]

Almost all aberrations except for field curvature are eliminated in ME–SV2 and ME–SU2. This aberration can be avoided by using a fiber–washer. Input surface of the washer is spherical. Its radius of curvature is equal to that of the objective focal surface (Figs. 1 and 2). Maximum diameter of the aberration circle does not exceed 10 μm over the whole field of view of the objective, in other words, this circle size is approximately one fourth of the area of a single element of the CCD matrix.

Calculational data on the parameters of this construction of ME–SV1 and ME–SU1 including radii of curvature, axial separations, and tables of aberrations are presented in Appendices 1 and 2 of Ref. 17, respectively. These parameters are given for six specific wavelengths (three in the visible and three in the VUV) corresponding to the centers of filter transmission bands in the case of imaging cameras for experiments with low apogee satellite orbiting at altitude of 800–1000 km. Comparing aberrations (Appendices 1 and 2 in Ref. 17) calculated for the visible and UV one can see, for instance, that maximum value of the spherical transverse aberration for two–mirror system is about 0.00774 mm in diameter at $\lambda = 630.0$ nm whereas for three–mirror system this parameter reaches its maximum at $\lambda = 184.0$ nm being 0.00904 mm. So, the aberration characteristics of ME–SU1 differ but slightly from those of ME–SV1 since both systems are concentric. Therefore, this type of optical systems is nearly achromatic. Our calculations demonstrate that ME–SV2 and ME–SU2 are achromatic too and aberration characteristics of this new modifications are close to those of the first modification since they differ only by the input correcting meniscus *1* (see Figs. 1 and 2) and by minimized screening of the input aperture. Hence, it is not reasonable to present these parameters here and we shall only describe them.

Objective ME–PV for the visible (Fig. 3) is composed of a concentric meniscus *1* with the radii of curvature of optical surfaces r_1 and r_2, convex–concave meniscus *2* with the radii of curvature r_3 and r_4, convex spherical mirror *3* with the radius of curvature r_5, concave spherical mirror *4* with the radius of curvature r_6, correcting meniscus *5* with the radii of curvature r_7 and r_8, Smith lens *6* with the radii r_9 and r_{10}, and a plane–parallel window *7* of the radiation detector. Spherical optical surfaces with the radii r_1, r_2, and r_3 are concentric with the common curvature center at the point *C* that coincides with the center of input pupil II. All lenses in the objective are made of quartz KV–R.

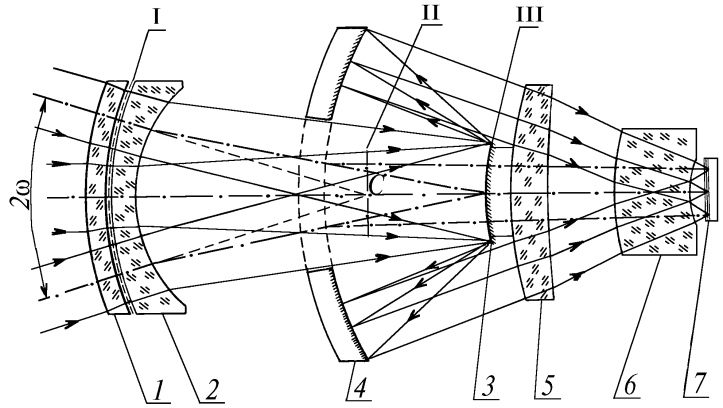

FIG. 3. Optical arrangement of ME–PV objective for the visible spectral region.

An important specific feature of this modification, similar to the previous ones, is combination of spheric interference filter I for selecting of specific emission line with either a concave surface radius r_2 of the concentric meniscus *1* or convex surface of radius r_3 of the meniscus *2*. Concentric meniscus *1*, similar to ME–SV2 and ME–SU2 modifications, serves as an input window protecting the interference filter against dangerous atmospheric and mechanical influence as well as against direct radiation.

Unlike to the modification ME–SV1 described in Refs. 17 and 21 and similar to the optical system used in ME–SV2 (see Fig. 1) the main specific feature of the objective ME–PV is minimization of screening of its central part due to a combination of the aperture diaphragm III with the outer frame of the convex mirror *3*. This provides an increase in the effective transmission of the objective and, hence, improvement in the threshold sensitivity of the imaging camera. It is of especial importance for measurements of distribution of low intensity emission from the upper atmosphere at middle latitudes when the exposure time is relatively short ranging from 0.1 to 0.2 s. That is especially important in the case when short–lived low–scale emissions against lower night ionosphere are monitored and separated against the "nightglow" background. This nightglow is caused by a powerful electromagnetic pulses generated by the ionospheric lightnings.[22]

A positive specific feature of the objective ME–PV is its plane image field formed by Smith lens *6* that corrects initial field curvature. This allows one to use conventional flat photocathode at the input of microchannel intensifier or flat input surface of fiber–washer for image recording. However, as it is seen from the table of aberrations presented in Appendix this objective is not achromatic in contrast to modifications ME–SV1 and ME–SV2 with the spherical image field. Parameters of ME–PV presented in Appendix were optimized for $\lambda = 630.0$ nm, therefore, the aberrations of the objective with the same parameters but at $\lambda = 486.1$ nm and 427.8 nm listed in the table of aberrations are appreciably higher. It should be pointed out in this connection, that parameters of the ME–PV optical system are to be calculated separately for each wavelength.

A convex spherical mirror *3* and correcting meniscus *5* are manufactured, in the objective ME–PV, as a single unit. To this end, the mirror *3* is stuck to the meniscus *5*, in other words, they are fixed by using deep optical contact. In that case, the correcting meniscus *5* serves also as an element providing rigid centering of the convex mirror *3* with respect to the concave mirror *4*.

Consider now the ray path in the objective ME–PV. A parallel beam is transformed by meniscus *1* and *2* (interference filter I is between these meniscus) in a diverging one. Then, it passes the central hole in the concave spherical mirror *4*, successively reflects from mirrors *3* and *4*, and passes the correcting meniscus *5*, Smith lens *6*, and input window of the detector *7*. The rays then converge on the photocathode forming a plane image.

Constructions of the objective ME–PV with reduced number of optical elements that have lower optical diameters and thickness are being currently studied. The modified optical system being achromatic should at the same time keep the image field plane. After such a design will be found the optical system at any wavelength in both the visible and the VUV (objective ME–PU) can be constructed that has aberration characteristics close to those of ME–SV.

3. CHARACTERISTICS OF AN IMAGING CAMERA SYSTEM FOR EXPERIMENTS FROM LOW APOGEE SATELLITE

Characteristics and configuration of a system of coaxial imaging cameras for low apogee satellite was described elsewhere[17] together with a detailed methodological basis.[17] It should be stressed here that this system is flexible and its configuration is not necessarily to be like the one presented in the table from Ref. 17, concerning the number of simultaneously observed emissions.

For solving a limited number of problems in the area of the remote diagnostics of ionospheric parameters considered in detail in Ref. 17, a set of four monochromatic cameras (1V, 2V, 1UV, 3UV) is used. These cameras have transmission bands centered at $\lambda = 630.0$ nm (OI), $\lambda = 427.8$ nm (N_2^+), $\lambda = 140.0$ nm (OI + N_2(LBH)), and $\lambda = 184.0$ nm (N_2(LBH)), respectively. It is also possible to use only two cameras (1UV and 3UV) or (1V and 2V) depending on specific parameters of a satellite orbit and a number of technical requirements of the project. It is essential that the fundamentals of the method are kept invariable, in other words, it is necessary to obtain intensity distribution of a pair of emissions from different altitude as was stated above. In contrast to the system configuration proposed in Ref. 17, the version presented here is composed of two threes or two pairs of imaging cameras that supplement each other with respect to the field–of–view angle in the direction across the flight trajectory. Indeed, instantaneous field–of–view angle in this direction is 63° with two cameras and 93° with three cameras (taking into account overlap of the fields of view of the adjacent cameras) whereas this angle is only 33° in the direction along the flight trajectory.

Figure 4 depicts an example of observation geometry for the system configuration composed of two bundles of imaging UV cameras. One bundle includes three cameras of 1UV type and another one consists of three cameras of 3UV type (Fig. 4 conditionally presents only one bundle of cameras). These cameras supplement each other with respect to the field–of–view angle in the direction across the flight trajectory, field–of–view angles of the adjacent cameras overlap approximately by 3°. The choice of cameras is related to the fact that spectral lines of N_2(LBH) at $\lambda = 184.0$ nm and OI at $\lambda = 135.6$ nm lying within the transmission bands of 3UV and 1UV cameras, respectively, are preferable for diagnostics of the ionospheric parameters[23,24] since one of the lines falls within the atmospheric absorption range with the maximum at $\lambda = 142.5$ nm and another one is out of this range. This approach makes the empirical relationship between E_0, F_e parameters and the intensity ratio (see above) independent of the upper atmosphere composition and, hence, calculations of the conductivity can be carried out more accurately.

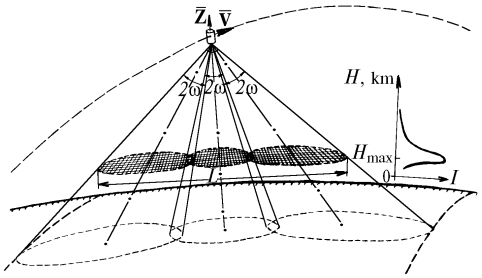

FIG. 4. Geometry of spectrophotometric measurements of characteristics of the polar ionosphere from a satellite by means of a panoramic system of a wide–angle monochromatic imaging cameras with the field–of–view angle $2\omega \approx 33°$. *Emission intensity as a function of altitude* $I = f(H)$ *and three image fields of cameras in one bundle at the altitude corresponding to maximum intensity* H_{max} *are depicted only as an example. Velocity vector is denoted by* **V**, **Z** *is the direction of building satellite axis to zenith. Spectral bands of cameras in this bundle are centered at* $\lambda = 140.0$ nm *and* 184.0 nm.

The system of cameras depicted in Fig. 4 allows panoramic mapping of intensity distribution of emissions from the upper atmosphere and measurement of ionospheric parameters with the spatial resolution of about 1 km and time resolution of about 1 s (see Ref. 17) in the region of $L \approx 1500$–1700 km (the length across the flight direction) and about 300–400 km in width (instantaneous value) along flight direction (at the altitude of emission). This region can correspond to both illuminated and dark hemispheres.

CONCLUSION

In our opinion the approach to construction of a system of monochromatic wide–angle imaging cameras on the basis of modifications of "monochromatic eye" objective presented in this paper enables one to reach the next stage in development of optics for remote diagnostics of the upper atmosphere and for technique of spectrophotometric investigations of characteristics of the aurora and parameters of the polar ionosphere as well as to carry out more accurate measurements from low apogee satellites.

The most important feature of the objective considered is a combination of its achromatism over a wide spectral range and a wide field–of–view angle at small aberrations over the whole field of view and, hence, with high spectral resolution. When changing interference filter at the input meniscus, one can adjust imaging camera to spectral range corresponding to a specific emission from the upper atmosphere selected with respect to specific physical problem and method of a particular experiment. We hope that the above–stated merits of the system of such imaging cameras mounted on a low apogee satellite will promote the collection of new data on physics of the upper atmosphere, the ionosphere, and on the physical processes in magnetosphere and ionosphere.

APPENDIX

Specifications of the ME–PV modification of the "monochromatic eye" objective.

Name of the system: concentric mirror and lens dualreflector with a meniscus compensator.

Type of the system	TYPE = 01
Location of an object	$S = \infty$, 0.0000
Angular dimensions of an object	$\omega = 16°30'$
Relative geometrical vignetting	$U_{\text{upper}} = 0.000$
	$U_{\text{lower}} = 0.000$
Location of the aperture diaphragm (AD)	
Number of surfaces before AD	$ND = 5.0$
Distance from AD to the preceding surface	$SD = 0$ mm
Central aperture (– front + back)	$AP = -7.2767$ mm $= -D/2 = -f'/2{:}1.25$ (D: $f' = 1{:}1.25$)
Location of the image plane	
Index of the surface setting	$IS = 0.0$
Parallax of the image plane setting (in mm from a Gaussian plane)	$SI = 0.03$ mm

Parameters of the construction.

Number of surfaces	Surface radii r, mm	Axial distances d, mm	Refractive indices of material $n(0)$ λ = 630 nm	$n(1)$ λ = 486.1 nm	$n(2)$ λ = 427.8 nm	Type of glass
			1.000000	1.000000	1.000000	
1	67.920	5.260	1.457104	1.463110	1.467356	Quartz KV–R
2	62.660	1.280	1.000000	1.000000	1.000000	
3	61.380	5.240	1.457104	1.463110	1.467356	Quartz KV–R
4	32.660	83.620	1.000000	1.000000	1.000000	
5	46.990	–38.550	–1.000000	–1.000000	–1.000000	
6	73.110	44.450	1.000000	1.000000	1.000000	
7	84.330	8.600	1.457104	1.463110	1.467356	Quartz KV–R
8	224.900	15.630	1.000000	1.000000	1.000000	
9	56.490	18.320	1.457104	1.463110	1.467356	Quartz KV–R
10	18.493	4.260	1.000000	1.000000	1.000000	
11	0.000	0.500	1.495550	1.502800	1.507800	S50–5M
12	0.000		1.000000	1.000000	1.000000	

Characteristics of the system in the paraxial region.

Total magnification V, mm	Back segment S', mm	Location of pupils: input S_p, mm	output S'_p, mm	Focal length: back f'_Σ, mm	front f_Σ, mm	Focal segment: back S'_f, mm	front S_f, mm
For λ_1 = 630.0 nm							
–18.4084	0.5006	67.9204	–128.0367	18.4041	–18.4041	0.4706	65.2846
For λ_2 = 486.1 nm							
–0.0063	–0.0267	67.6789	–126.5636	18.2875	–18.2875	0.4739	65.0464
For λ_3 = 427.8 nm							
–0.0100	–0.0247	67.5095	–125.5493	18.2058	–18.2058	0.4759	64.8794

A point is on the axis. Central aperture: front $A = 7.2767$ mm, back $A' = 0.3952$ (sin σ').

Coordinate at the input h_i, mm	Spherical aberration: longitudinal Δs', mm	Spherical aberration: transverse Δy', mm	Wave aberration W, μm	Nonisoplanatism η, %	Coordinate at the output tan σ'
For $\lambda_1 = 630.0$ nm					
7.2767 $(4/4)^{1/2}$	−0.00188	−0.00080	−0.50045	0.02559	0.43021
7.2767 $(2/4)^{1/2}$	−0.00155	−0.00045	−0.53802	0.01747	0.29106
For $\lambda_2 = 486.1$ nm					
7.2767 $(4/4)^{1/2}$	−0.01060	−0.00459	−0.70541	−0.62509	0.43357
7.2767 $(2/4)^{1/2}$	−0.00367	−0.00107	−0.51856	0.62760	0.29310
For $\lambda_3 = 427.8$ nm					
7.2767 $(4/4)^{1/2}$	−0.01722	−0.00750	−0.88559	−1.08610	0.43597
7.2767 $(2/4)^{1/2}$	−0.00555	−0.00163	−0.51870	−1.08457	0.29456

The point is out of axis.
Principal ray. Dimensions of an object: ω = 16°30'.
Vignetting: $U_{upper} = 0.000$, $U_{lower} = 0.000$.

Dimensions of an image y', mm	Distortion Δ, %	Location of pupils: input S_p, mm	Location of pupils: output S'_p, mm	Astigmatic segments: z'_t, mm	Astigmatic segments: z'_s, mm
For $\lambda_1 = 630.0$ nm					
−5.16469	−5.28403	67.88144	−120.05937	−0.02662	−0.03546
For $\lambda_2 = 486.1$ nm					
0.03187	−5.86859	67.64258	−188.78851	−0.02603	−0.03190
For $\lambda_3 = 427.8$ nm					
0.05420	−6.27818	67.47475	−117.91800	−0.02590	−0.02972

REFERENCES

1. C.–I. Meng, R.E. Huffman, R.A. Skrivanek, et al., SPIE. Ultraviolet Technology **687**, 62–72 (1986).
2. M. Ishimoto, C.–I. Meng, G.J. Romick, and R.E. Huffman, J. Geophys. Res. **93**, No. A9, 9854–9866 (1988).
3. R.R. Vondrak and R.M. Robinson, in: *Abstracts of Reports at 40th Congress of the International Astronautical Federation*, IAF–89–179, Malaga, Spain (1989).
4. M.H. Rees, D. Lummerzheim, R.G. Roble, et al., J. Geophys. Res. **93**, No. A11, 12841–12860 (1988).
5. V.A. Gladyshev, A.K. Kuzmin, T.M. Mularchik, et al., Ann. Geophys. **38**, No. 5, 631–634 (1982).
6. M.M. Gogoshev, N. Petkov, A.K. Kuzmin, et al., Adv. Space Res. **2**, No. 7, 115–120 (1983).
7. E. Kaneda, T. Mukai, and K. Hirao, in: *Geophys. Monogr. Ser. Vol. 25. Physics of Auroral Arc Formation,* ed. by S.–I. Akasofu and J.R. Kan, pp. 24–30 (1981).
8. L.A. Frank, J.D. Craven, K.L. Ackerson, et al., Space Sci. Instr. **5**, No. 4, 369–393 (1981).
9. C.I. Meng and R.E. Huffman, Geophys. Res. Lett. **11**, 315–318 (1984).
10. F.W. Schenkel, B.S. Ogorzalek, J.C. Larrabee, et al., Appl. Opt. **24**, No. 20, 3395–3405 (1985).
11. C.D. Anger, S.K. Babey, A.L. Broadfoot, et al., Geophys. Res. Lett. **14**, No. 4, 387–390 (1987).
12. T. Oguti, E. Kaneda, M. Ejiri, et al., J. Geomagn. Geoelectr. **42**, No. 4, 555–564 (1990).
13. M. Andre, ed., *The FREJA Scientific Satellite. The FREJA Science Team* (Swedish Institute of Space Physics, Kiruna, Sweden, 1991), 190 pp.
14. L.L. Cogger, Yu.I. Galperin, G.G. Shepherd, et al., in: *Project Interball*, ed. by CNES, France (1995), pp. 267–272.
15. R.B. Johnson, Opt. Eng. **27**, No. 12, 1046–1050 (1988).
16. G.M. Popov, *Concentric Optical Systems and Their Applications in Optical Design* (Nauka, Moscow, 1969), 136 pp.
17. A.K. Kuz'min and K.N. Chikov, Kosmich. Issled. **32**, No. 1, 126–142 (1994).
18. D.S. Volosov, *Technique for Calculations of Complex Photographic Systems* (Gostekhizdat, Leningrad–Moscow, 1948), 394 pp.
19. Yu.G. Yakushenkov, V.N. Lukantsev, and M.P. Kolosov, *Methods of Jamming Control in Opto–Electronic Devices* (Radio i Svyaz', Moscow, 1981), 180 pp.
20. M. Zukic, D.G. Torr, J. Kim, J.E. Spann, and M.R. Torr, Opt. Eng. **32**, No. 12, 3069–3074 (1993).
21. A.K. Kuzmin and K.N. Chikov, in: *Proceedings of the 19th Annual European Meeting on Atmospheric Research by Optical Methods*, Kiruna, Sweden (1992), pp. 585–592.
22. W.L. Boeck, O.H. Vaughan, R. Blakeslee, B. Vonnegut, and M. Brook, Geophys. Res. Lett. **19**, 99–102 (1992).
23. G.A. Germany, M.R. Torr, P.G. Richards, and D.G. Torr, J. Geophys. Res. **95**, No. A6, 7725–7733 (1990).
24. G.A. Germany, M.R. Torr, D.G. Torr, and P.G. Richards, J. Geophys. Res. **99**, No. A1, 383–388 (1994).